

Silicon Micromachined Millimeter-Wave Turnstile Orthomode Transducer

Adrian Gomez-Torrent, *Student Member, IEEE*

Abstract—Abstract goes here.

I. INTRODUCTION

THERE is an increasing interest in millimeter wave (mmW) receivers for remote sensing in earth and space observation missions [1]. These receivers require orthomode transducers (OMT) to discriminate between the two orthogonal polarizations present in the receiving antenna. At mmW frequencies fabrication becomes a big challenge as a consequence of the complex geometry of OMTs and the reduced dimensions of waveguides.

The Bøifot [2], and the turnstile junction [3] are the most frequently used OMT designs due to their twofold symmetrical geometry that allows broadband operation up to a theoretical 60% fractional bandwidth (FBW) [4]. This is achieved by avoiding the excitation of higher order TE_{11} and TM_{11} modes in the common square waveguide port. However, the twofold symmetry increases the fabrication complexity due to the required recombination networks.

An approach to simplify the fabrication for the mmW frequency range is to use onefolded symmetrical geometries that allow simpler split block fabrication at the cost of a reduced operation bandwidth [5]–[7]. The authors in [6] used high precision CNC-milling to implement an asymmetrical side-arm OMT working from 500 – 600 GHz. Even though they reported good RF performance (see Table I), the paper claimed difficulty to achieve good isolation levels due to misalignments between the two metal blocks, and stated that alternative fabrication techniques for the fabrication of high frequency OMTs would be beneficial. Later they presented a multi-step silicon micromachining process on a similar OMT geometry [7], obtaining superior RF performance in terms of insertion loss and cross polarization due to an improved fabrication accuracy, that would also allow high density integration and batch fabrication.

However, many applications requiring full waveguide-band operation (40% FBW) need the more complex twofold symmetrical OMTs mentioned before. Bøifot OMTs have been broadly used at frequencies above 100 GHz since they only require one recombination network, in contrast to turnstile

OMTs. Therefore, Bøifot OMTs can be fabricated in a split-block configuration by high-precision machining for broadband applications [8]–[11].

The authors in [8] implemented a classical Bøifot OMT in a split-block configuration by electric-discharge-machining (EDM), fabricating the septum as a separate piece photolithographically patterned, and the shorting posts made of copper-stainless steel wire. The OMT in [9] was also fabricated in a split-block configuration by CNC-milling, implementing the septum with a separately machined copper sheet, and replacing the shorting pins with a stepped impedance transformer. Apart from the high precision machining required for these structures, fabrication and assembly of the septum further increases the fabrication complexity of broadband OMTs. The authors in [10], [11] avoided the use of a septum by using reverse-coupling and double-ridged architectures respectively, which limited the operation bandwidth below a 30% FBW. While these four works reported excellent RF performance (see Table I) at very high frequency (up to 500 GHz), the fabrication of such high-precision machined parts is very challenging and expensive, and the resulting components are heavy and bulky solid metal blocks.

Turnstile OMTs have a more complex architecture since a recombination network is needed for each polarization. The standard approach for the fabrication of such component is to divide it in four blocks intersecting along the common waveguide port axis [3], that was also reported in [12] for the 200 – 270 GHz frequency band. The authors of this work fabricated five identical devices in a four-block configuration using different metals and different machining techniques, and although some of the devices showed good performance (see Table I), several alignment and gap issues were described in the paper that required manual filling of the metal gaps in order to achieve the reported performance.

Some alternative techniques for the fabrication of turnstile OMTs have also been developed in the W-band [13], [14], using electroforming and wire erosion respectively. The authors in [14] divided the OMT geometry in several layers, with simple 2D geometries on each layer that were defined by wire erosion on metal plates. These plates were stacked, resulting in a very compact component, with high performance, and with the possibility of batch production and dense integration. However, this fabrication technique would be difficult to scale up in frequency due to the thin metal sheets that would be required.

The turnstile OMT presented in this work was designed for operation in the full WM864 band, 220 – 330 GHz, being the first micromachined broadband OMT to the authors knowledge. Preliminary measurement results with open-

This paper is an expanded version from the IEEE MTT-S International Microwave Symposium (IMS2018), Philadelphia, PA, USA, June 10-15, 2018.

The authors are with the Department of Micro and Nanosystems, School of Electrical Engineering and Computer Science, KTH Royal Institute of Technology, Stockholm SE-100 44, Sweden

The contribution by KTH to this work has received funding from the European Research Council (ERC) under the European Union's Horizon 2020 research and innovation programme (grant agreement No 616846), and the Swedish Foundation for Strategic Research Synergy Grant Electronics SE13-007.

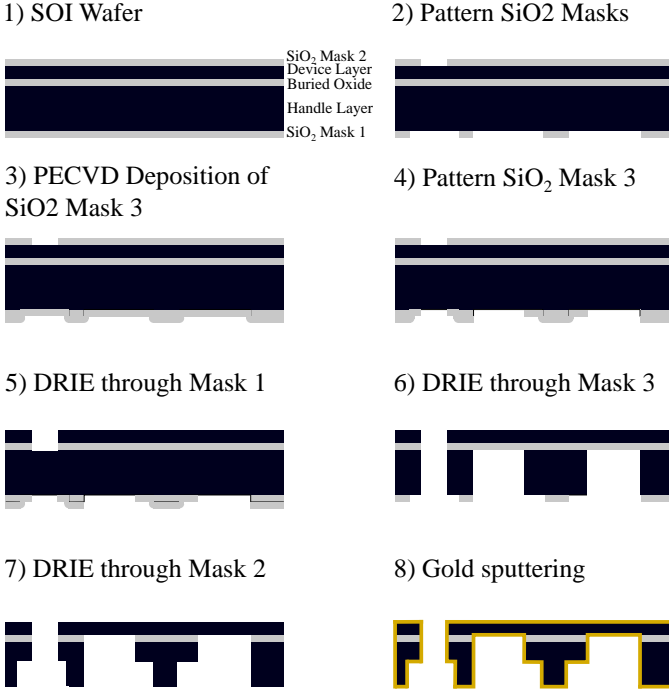
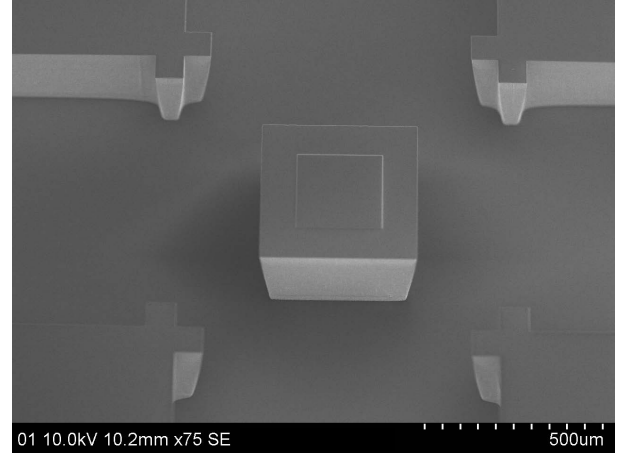


Fig. 1: Fabrication process flow for the turnstile junction of the OMT.

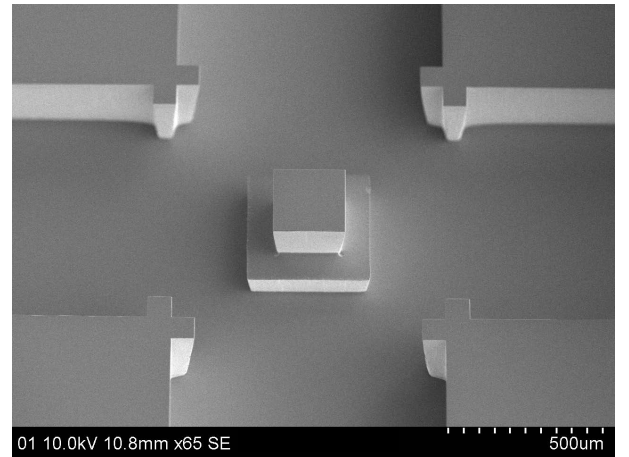
ended and shorted common-port configurations were already shown in [15]. These preliminary measurements were done to evaluate the fabrication approach, since the reduced size of the component in comparison with the test-port flange size makes its full characterization very challenging. For this extended paper, further fabrications have been carried out with new layout designs that allow the full electromagnetic characterization of the OMT, including insertion loss, and return loss for both polarizations and cross polarization levels.

II. FABRICATION PROCESS

Deep reactive ion etching (DRIE) of silicon-on-insulator (SOI) wafers has already proven to be an accurate fabrication technology for low-loss waveguides at millimeter-wave frequencies [16]. The SOI wafers in this work are made of a $275\mu\text{m}$ silicon handle layer, bonded to a $30\mu\text{m}$ silicon device layer with a $3\mu\text{m}$ buried oxide (BOX) layer in between, see Fig.1. The handle layer is used to define the waveguide channels, the BOX acts as an etch stop, and the device layer forms the bottom wall of the waveguide. In comparison to standard silicon wafer etching [7], the SOI structure gives well-defined sharp corners between the lateral walls of the waveguide and the bottom layer, that has a nanometre-scale surface roughness, dramatically decreasing the insertion loss of the component without the requirement of any further post-processing steps. Well known microfabrication techniques such as multi-step silicon etching, bottom-side mask alignment, or thermo-compression bonding of several chips allow to increase the design complexity of waveguide components, including out of plane bends, stepped transitions, and complex recombination networks.



(a)



(b)

Fig. 2: SEM picture of turnstile junction (a) after first etching step in handle layer, and (b) after second etching step in handle layer.

The detailed process flow for the OMT fabrication is shown in Fig.1. The wafers are first thermally oxidized to form a $2\mu\text{m}$ silicon oxide film in both sides of the wafer, these are used as hard-masks for the deep silicon etching process. The mask pattern is transferred to the wafer by photolithography using backside alignment and the oxide layer is dry etched in a SPTS Advanced Oxide Etching tool. A $2\mu\text{m}$ silicon oxide layer is deposited on the handle layer using plasma enhanced chemical vapour deposition (PECVD) to form the third hard mask that will allow to etch two different heights. Then the third mask pattern is transferred to the PECVD oxide as described before, leaving Mask 2 buried below the deposited oxide.

The silicon etching is performed in an Applied Materials Centura Etch tool, that uses the Bosch process for deep silicon etching. The selectivity of the process over the silicon oxide mask is over 150:1, allowing the etching of deep trenches with a high resolution due to the thin mask required. The device layer is first etched down to the BOX layer. Then the handle layer is etched through Mask 3 forming the waveguide channels. After this etching step the few nanometres left from Mask 3 are removed with plasma etching to expose Mask 2

and perform the last silicon etching step, this time not through the whole handle layer, but to a depth of $180\mu\text{m}$. This process allows to very accurately define the height of both steps, since they are totally independent, and etching time variations for the second step will not change the depth of the first one. Fig.2 shows a scanning electron microscope (SEM) image of the turnstile junction before and after the second etching step of the handle layer. Note that Mask 2 can be seen in Fig.2(a) and it will define the second step of the post, while the rest of the geometry remains unchanged after the second etching step.

Finally the individual chips are cleaned in an oxygen plasma oven and metallized with a $2\mu\text{m}$ thick gold layer in a sputtering tool. The skin depth at the lowest frequency of operation for gold is $\delta_s = 160\text{nm}$, so the metal layer is thicker than ten times the skin depth. The OMTs are then assembled by stacking the three chips in a custom made holder for alignment and thermal-compression bonded at 250°C and 2.5N m for 1 hour.

III. DESIGN

The design of turnstile orthomode transducers has been extensively discussed in the literature (see [3], [17] among others), therefore this section will describe the specific considerations regarding the design of such components at mmW frequencies for silicon micromachining. The constraints considered for the design are: (1) in-plane waveguides must have a $275\mu\text{m}$ height, set by the handle layer thickness in the SOI wafer; (2) the scatterer post can have a maximum height of $275\mu\text{m}$; and (3) all out-of-plane steps must have the same height. On the other hand, there is total design freedom for the in-plane geometries on the chip, since they are transferred to the wafer through a photolithography step, and thus complex shapes in that plane are accurately realized with no added difficulty. CST Microwave Studio was used for the individual design of each sub-component in the OMT. A target of 25dB return loss for the whole band was set to avoid reflections when cascading the components to each other.

The turnstile junction was first designed formed by a $864\mu\text{m} \times 864\mu\text{m}$ square waveguide that ends in four $275\mu\text{m} \times 864\mu\text{m}$ reduced height waveguides, with a two-stepped square scatterer post in the center, see Fig.3 (a). The post acts as a tuning stub to achieve the required matching, and the step height was set to $95\mu\text{m}$. Due to the height limitation for the post, inductive irises were added to each rectangular waveguide to further improve the return loss.

The junction alone needs a three SOI stack for its fabrication, as shows in Fig.3 (a), therefore efforts were made to implement the recombination networks using these three chips. Fig.3 (b) shows the final geometry of the OMT that is split in three wafers, with 2 different steps each. Each polarization is re-routed either in Chip 1 or Chip 3, while Chip 2 is used to implement the impedance transformers for the E-plane power combiners and the out of plane bends. The simulated return loss for the H-plane bends, E-plane bends, E-plane power combiner, and turnstile junction are shown in Fig.4. Some of the components were re-optimized after cascading them to

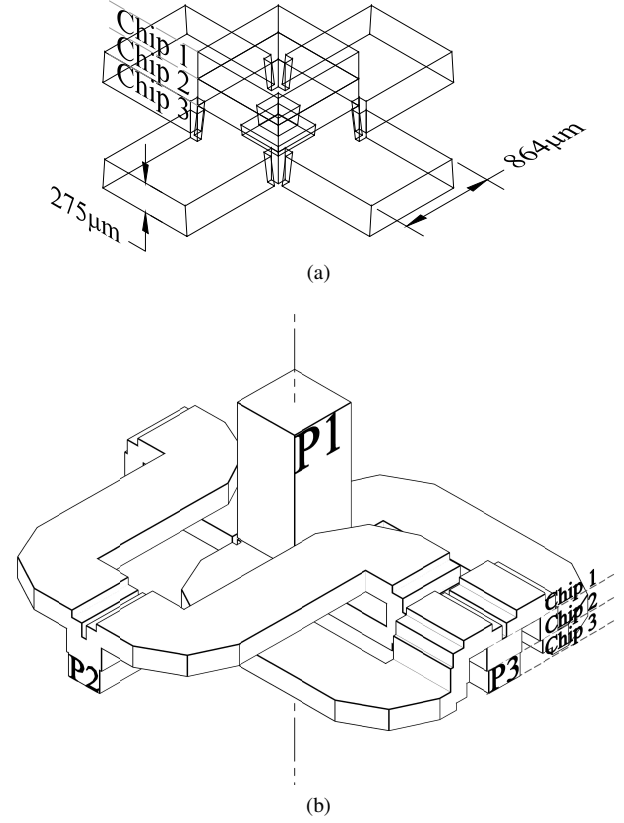


Fig. 3: 3D drawings of (a) turnstile junction, and (b) complete OMT.

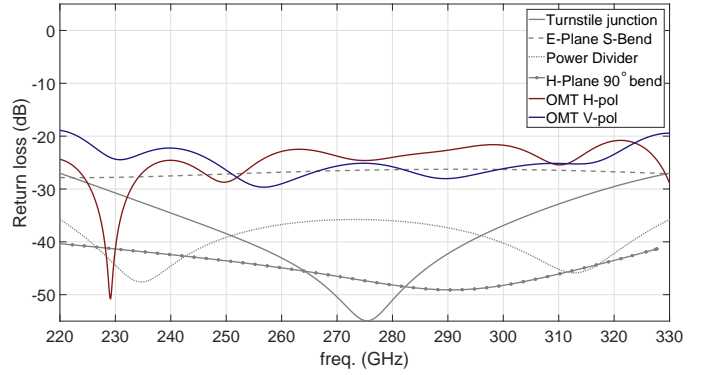


Fig. 4: Simulated return loss of individual components and both polarizations of OMT.

form the OMT, and the final return loss for both polarization channels is depicted in Fig.4.

IV. MEASUREMENT SETUP

Two chip layouts were designed to facilitate different measurements: a $10\text{mm} \times 10\text{mm}$ chip, which was shown in [15] and allows for connecting to the rectangular ports, and a full flange size $20\text{mm} \times 20\text{mm}$ chip, shown in Fig.5 (d), allowing connection to the square port. The first solution enabled simple measurements of the return loss by leaving the square port open, and a first estimation of the insertion loss and cross polarization level by shorting that port. The

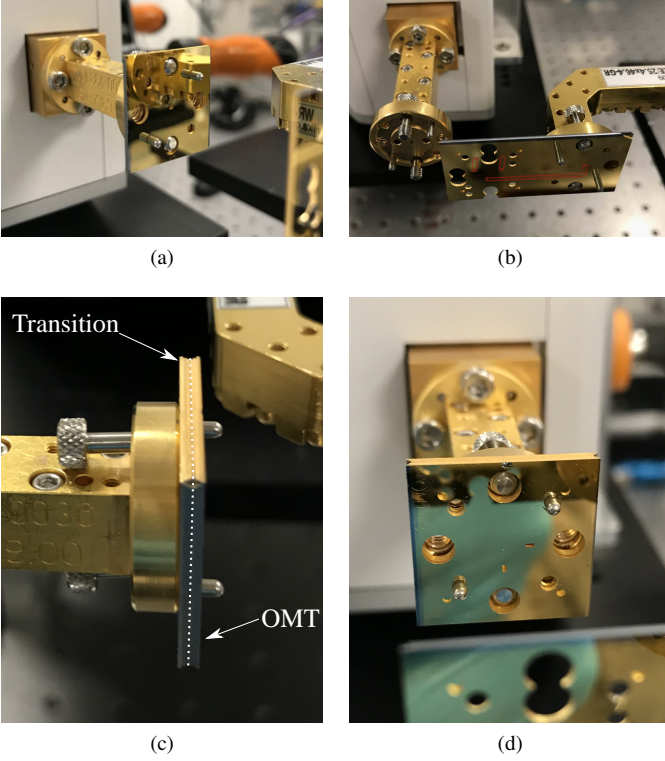


Fig. 5: Measurement setup pictures showing: (a) silicon micro-machined rectangular to square waveguide transition mounted on test port, (b) silicon micromachined test fixture with outlined waveguide section and two matched loads, (c) side-view of transition and OMT mounted on test port, and (d) OMT with two output ports.

second chip layout provides access to the three ports of the OMT, but requires the use of two additional test components to connect the OMT to the vector network analyzer (VNA). All devices are fabricated with elliptical alignment holes, as described in [18], to ensure repeatable and accurate alignment between the silicon micromachined chips and the CNC-milled standard test ports.

The first test device is a rectangular to square waveguide transition for independently characterizing each channel of the OMT, shown in Fig.5 (a). The transition is designed to be manufactured in the same fabrication run as the OMT, and thus, it is composed of three stacked SOI chips forming a six-step transition. Fig.6 shows a drawing of the design including the dimensions for both waveguide ports and the simulated return loss, better than 25 dB for the whole band. Two identical transitions were fabricated (T1 and T2) and measured with an open-ended square port. The measured return loss agrees well with the re-simulated data that takes into account the effect of the open ended square port, see Fig.6.

The second test device, shown in Fig.5 (b), is a 40 mm x 20 mm chip that routes one of the rectangular ports in the OMT to the VNA, and loads the other one with a matched absorber. The layout of this test fixture (TF) enables the characterization of the insertion and return loss for both channels while loading the isolated port, and measurement

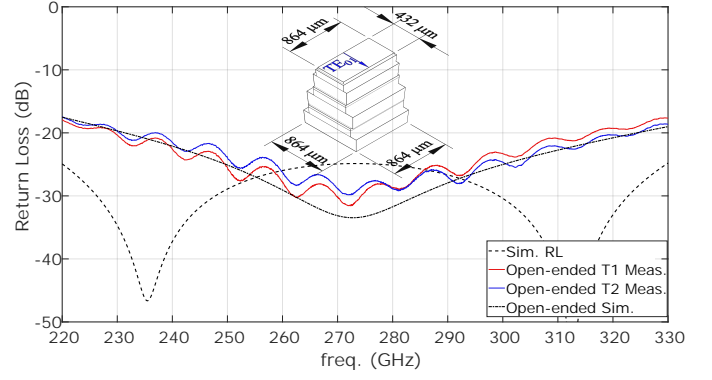


Fig. 6: 3D drawing of rectangular to square waveguide transition and simulated return loss (dashed line). Measured and simulated return loss with an open-ended square port for two fabricated prototypes (T1 and T2).

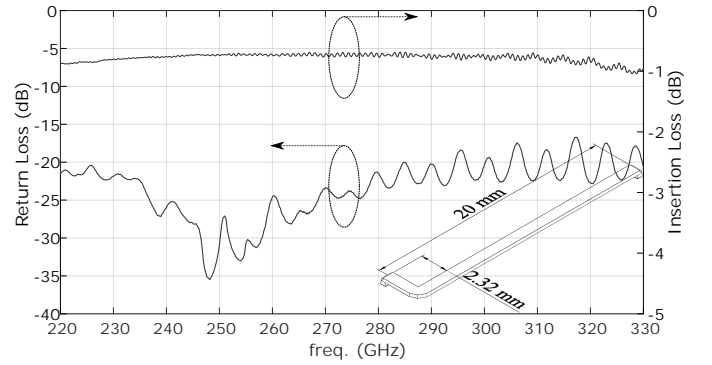


Fig. 7: 3D drawing of the waveguide section embedded in the test fixture and measured S-parameters.

of the cross-polarization level while loading the direct port. The waveguide section and two loads are outlined in Fig.5 (b). Note that the TF includes a second set of alignment and screw holes with an offset to be able to measure the S-parameters of the waveguide section and deembed it from the OMT measurement results.

The matched loads were fabricated by micromachining low resistivity silicon taper geometries that are inserted in the silicon micromachined waveguide channel, as described in [19]. Fig.7 shows a 3D drawing of the waveguide section and the measured S-parameters, that include two E-plane bends and a H-plane bend. The measured insertion loss is always kept below 1 dB for the 23 mm waveguide section, that corresponds to better than 0.045 dB/mm, this results are in good agreement with our previous data shown in [16].

The measurements are performed by cascading these three components as shown in Fig.5. First the transition and the OMT are mounted in port 1 (P1), therefore loading one of the channels in the OMT (Fig.5 (c)). Then the TF is mounted in port 2 (P2, Fig.5 (b)) and connected to the OMT in P1 (Fig.5 (d)). In this configuration, the measured S parameters correspond to the insertion loss and return loss of one of the OMT channels once the TF is deembedded. Note that the rectangular to square transition is not deducted from the measurements, therefore it is included in the simulated data shown in section

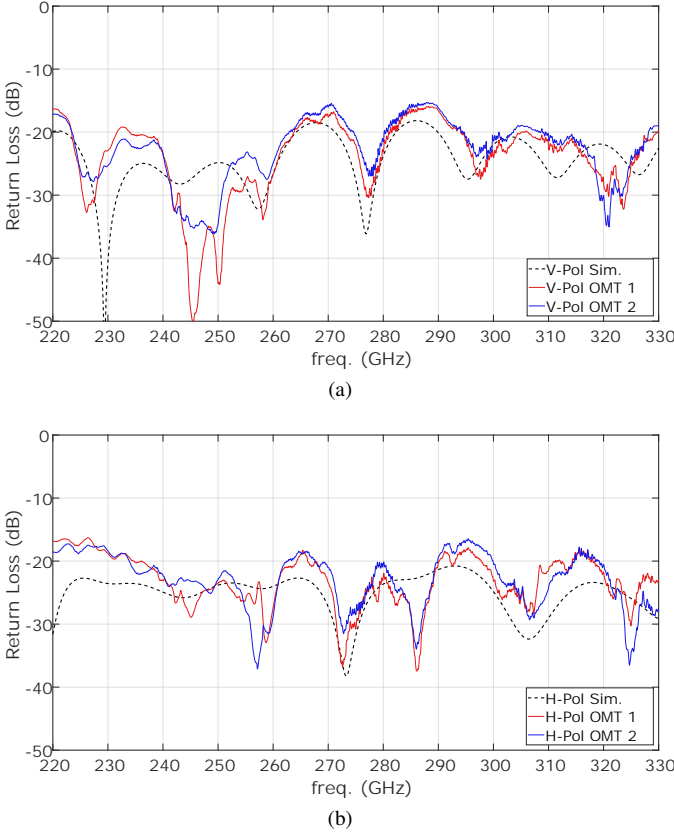


Fig. 8: Measured vs. simulated return loss for both fabricated OMT prototypes: (a) vertical polarization channel, and (b) horizontal polarization channel.

V. The other OMT channel is measured by rotating the OMT chip 90° along the square port axis. Any power leaked to the isolated channel due to cross polarization or misalignment between the transition and the OMT is terminated in one of the two matched loads included in the TF chip. Finally, the cross polarization level is measured by rotating the test port P1 and the transition 90° along the propagation axis with respect to the OMT. This configuration loads with P1 the OMT channel that is terminated in the TF, and the isolated port is connected to the waveguide section that goes to P2 in the VNA. Therefore the measured S_{21} corresponds to the cross-polarization level.

V. MEASUREMENT RESULTS

A Rohde & Schwarz ZVA-24 VNA with ZC330 frequency extenders was used for the RF characterization of the component. The reference planes for the measurements were set in the waveguide test ports using a through-open-short-match (TOSM) 2-port calibration. Two OMT prototypes were fabricated in two separate batches, they were characterized and the results are presented and discussed in this section. The results are also compared in Table I with the OMTs at mmW frequencies cited in section I, that were considered to be the most representative high frequency OMT results to date.

The reflection measurements for both polarizations are shown in Fig.8, along with the simulated data. Note that the OMT has been re-simulated to consider the effect of the

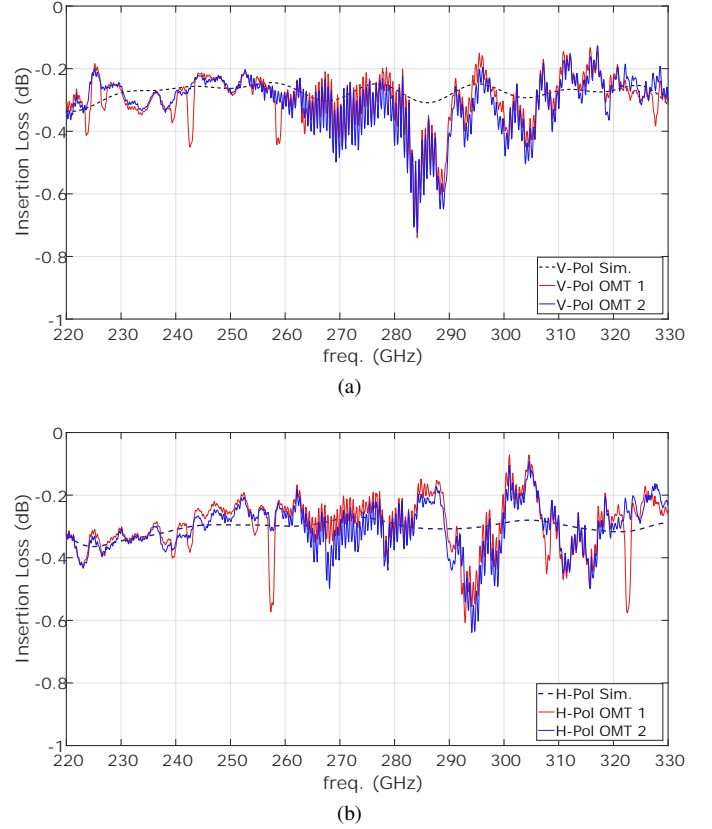


Fig. 9: Measured vs. simulated insertion loss for both fabricated OMT prototypes: (a) vertical polarization channel, and (b) horizontal polarization channel.

rectangular to square waveguide transition, which does not strongly deteriorate its RF performance. The measured return loss is better than 16 dB for both polarizations over the whole waveguide band, with an average value of 22 dB. Fig.9 shows the insertion loss for both OMTs, always better than 0.6 dB with an average value better than 0.3 dB for both polarizations in any of the OMTs.

The cross polarization level for both OMTs is shown in Fig.10. The average cross polarization level is above 50 dB for OMT 1, and above 60 dB for OMT 2. Due to the perfect twofold symmetry of the turnstile junction, the simulated cross polarization is above 70 dB, however some spikes are present in both devices that deteriorate the performance to a 20 dB and 30 dB cross polarization level respectively. These spikes in the cross polarization are also reflected in OMT 1 as sharp signal drop-outs shown in Fig.9. No noticeable S_{21} drop-outs are observed in the measurements of OMT 2, which can be attributed to a lower level of the spikes in the cross polarization, hence smaller signal drop-outs could be masked by the noise present in the measurements.

The different factors contributing to these spikes were studied by the authors in [20], where most of them are a direct consequence of fabrication nonidealities. Some of these factors, such as the symmetry of recombined branches or gaps along waveguide seams are not applicable for the silicon micromachining approach used for this work, due to

TABLE I: Comparison of mmW OMTs published previous to this work

Reference	Device	Frequency Range	Return Loss	Insertion Loss	Isolation	Fabrication Technology
[5]	Side-arm	78 – 102 GHz (26% FBW)	> 24 dB	< 0.4 dB	> 37 dB	CNC-milling
[6]	Side-arm	500 – 600 GHz (18% FBW)	> 17 dB	< 5 dB	> 25 dB	CNC-milling
[7]	Side-arm	500 – 600 GHz (18% FBW)	> 10 dB	< 2 dB	> 25 dB	Silicon Micromachining
[8]	Bøifot	200 – 300 GHz (40% FBW)	> 15 dB	< 0.75 dB	> 40 dB	Electric Discharge Machining
[9]	Bøifot	180 – 270 GHz (40% FBW)	> 27 dB	< 0.7 dB	> 41 dB	CNC-milling
[11]	Bøifot	125 – 163 GHz (26% FBW)	> 18 dB	< 0.5 dB	> 28 dB	CNC-milling
[10]	Bøifot	385 – 500 GHz (26% FBW)	> 10 dB	< 3.25 dB	> 25 dB	CNC-milling
[12]	Turnstile	210 – 290 GHz (32% FBW)	> 12 dB	< 1 dB	> 25 dB	CNC-milling
[13]	Turnstile	75 – 110 GHz (19% FBW)	> 16 dB	< 1 dB	> 45 dB	Electroforming
[14]	Turnstile	79.9 – 108.1 GHz (30% FBW)	> 20 dB	< 0.25 dB	> 42 dB	Wire Erosion
This work	Turnstile	220 – 330 GHz (40% FBW)	> 16 dB	< 0.6 dB	> 30 dB	Silicon Micromachining

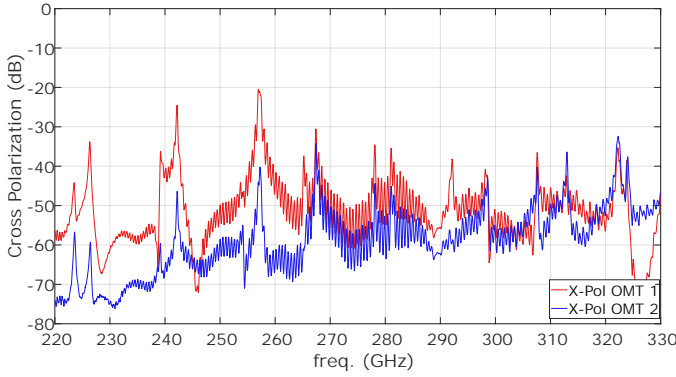


Fig. 10: Cross polarization levels for both fabricated OMT prototypes.

the photolithographic patterning accuracy and the chip-to-chip bonding process that avoids any gaps, see section II. However, misalignment between the chips in the stack could be a major issue, specially for the turnstile junction.

The misalignment between all chips for both OMTs were measured to study its influence on the cross-polarization level. Alignments better than $5\mu\text{m}$ were measured between all chips using Vernier scales implemented on the corners of each chip. The worst case alignment is shown in Fig.11, which corresponds to OMT 1. Both OMTs were re-simulated including the measured misalignments, and while the return loss performance is not affected by these small misalignments in this frequency range, simulation data shows that the cross polarization can be strongly deteriorated, as shown in Fig.12.

VI. CONCLUSIONS

The complete RF characterization of a silicon micromachined turnstile OMT working in the full WM864 band, (220 – 330 GHz), is presented for first time in this work. The measured performance for the best OMT prototype, with better than 16 dB return loss, 0.6 dB insertion loss, and 30 dB cross polarization, is superior to previously reported silicon micromachined OMTs, and comparable to the best CNC-milled components above 200 GHz known to the authors, see Table I. The design uses a three-chip stack with a maximum of two etch-depths to implement the complex geometry required

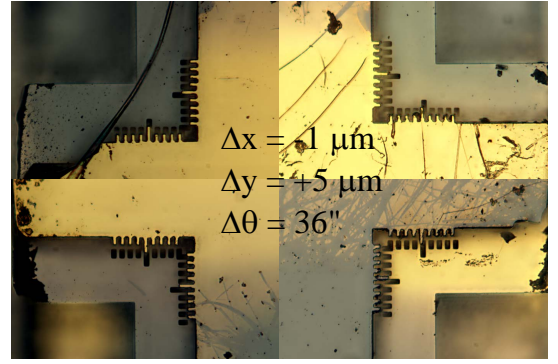


Fig. 11: Chip1-to-Chip2 misalignment for OMT 1 after bonding.

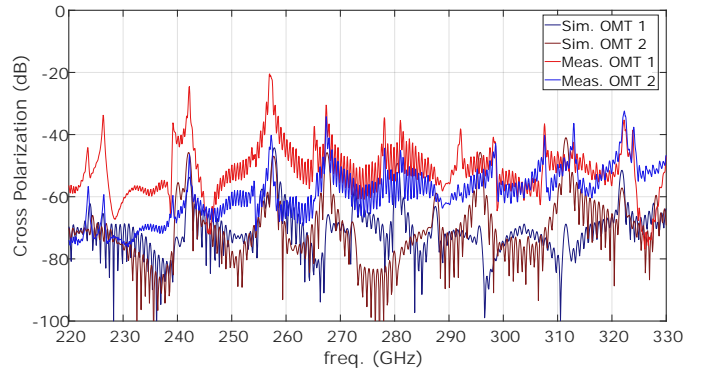


Fig. 12: Comparison of cross polarization levels for both fabricated OMT prototypes with simulated data including the effect of the measured misalignment.

for turnstile OMTs, that after bonding, results in a compact 20 mm x 20 mm x 1 mm size device. The reduced footprint of the component, the coplanar output port arrangement, and the ability for low-cost batch fabrication combined with high performance, makes silicon micromachining of turnstile OMTs a promising technology enabling integration of multi-pixel systems.

REFERENCES

- [1] M. C. Carter, A. Baryshev, M. Harman, B. Lazareff, J. Lamb, S. Navarro, D. John, A.-L. Fontana, G. Ediss, C. Y. Tham, *et al.*, "ALMA front-

- end optics,” in *Ground-based Telescopes*, vol. 5489, pp. 1074–1085, International Society for Optics and Photonics, 2004.
- [2] A. Bøifot, E. Lier, and T. Schaug-Pettersen, “Simple and broadband orthomode transducer,” in *IEE Proceedings H (Microwaves, Antennas and Propagation)*, vol. 137, pp. 396–400, IET, 1990.
 - [3] A. Navarrini and R. L. Plambeck, “A turnstile junction waveguide orthomode transducer,” *IEEE Transactions on Microwave Theory and Techniques*, vol. 54, pp. 272–277, Jan 2006.
 - [4] J. A. Ruiz-Cruz, J. R. Montejo-Garai, C. A. Leal-Sevillano, and J. M. Rebollar, “Ortho-mode transducers with folded double-symmetry junctions for broadband and compact antenna feeds,” *IEEE Transactions on Antennas and Propagation*, 2018.
 - [5] A. Dunning, S. Srikanth, and A. Kerr, “A simple orthomode transducer for centimeter to submillimeter wavelengths,” in *20th International Symposium on Space Terahertz Technology, Charlottesville*, pp. 20–22, 2009.
 - [6] T. J. Reck and G. Chattopadhyay, “A 600 GHz asymmetrical orthogonal mode transducer,” *IEEE Microwave and Wireless Components Letters*, vol. 23, no. 11, pp. 569–571, 2013.
 - [7] C. Jung-Kubiak, T. J. Reck, J. V. Siles, R. Lin, C. Lee, J. Gill, K. Cooper, I. Mehdi, and G. Chattopadhyay, “A multistep DRIE process for complex terahertz waveguide components,” *IEEE Transactions on Terahertz Science and Technology*, vol. 6, no. 5, pp. 690–695, 2016.
 - [8] E. Wollack and W. Grammer, “Symmetric waveguide orthomode junctions,” in *Proceedings of the 14th International Symposium on Space TeraHertz Technology*, pp. 169–176, NRAO, 2003.
 - [9] C. A. Leal-Sevillano, T. J. Reck, G. Chattopadhyay, J. A. Ruiz-Cruz, J. R. Montejo-Garai, and J. M. Rebollar, “Development of a wideband compact orthomode transducer for the 180–270 GHz band,” *IEEE Transactions on Terahertz Science and Technology*, vol. 4, no. 5, pp. 634–636, 2014.
 - [10] A. Navarrini, C. Groppi, and G. Chattopadhyay, “A waveguide orthomode transducer for 385–500 GHz,” in *Millimeter, Submillimeter, and Far-Infrared Detectors and Instrumentation for Astronomy V*, vol. 7741, pp. 7741–7786, 2010.
 - [11] S. Asayama and M. Kamikura, “Development of double-ridged waveguide orthomode transducer for the 2 mm band,” *Journal of Infrared, Millimeter, and Terahertz Waves*, vol. 30, pp. 573–579, Jun 2009.
 - [12] A. Navarrini, A. Bolatto, and R. L. Plambeck, “Test of 1 mm band turnstile junction waveguide orthomode transducer,” in *Proc. 17th Int. Symp. STT*, pp. 99–102, 2006.
 - [13] G. Pisano, L. Pietranera, K. Isaak, L. Piccirillo, B. Johnson, B. Maffei, and S. Melhuish, “A broadband WR10 turnstile junction orthomode transducer,” *IEEE Microwave and Wireless Components Letters*, vol. 17, no. 4, pp. 286–288, 2007.
 - [14] G. Virone, O. A. Peverini, M. Lumia, M. Z. Farooqui, G. Addamo, and R. Tascone, “W-band orthomode transducer for dense focal-plane clusters,” *IEEE Microwave and Wireless Components Letters*, vol. 25, no. 2, pp. 85–87, 2015.
 - [15] A. Gomez-Torrent, U. Shah, and J. Oberhammer, “Wideband 220 – 330 GHz turnstile OMT enabled by silicon micromachining,” in *Microwave Symposium (IMS), 2018 IEEE MTT-S International*, pp. 1–4, IEEE, 2018.
 - [16] B. Beuerle, J. Campion, U. Shah, and J. Oberhammer, “A Very Low Loss 220-325 GHz Silicon Micromachined Waveguide Technology,” *IEEE Transactions on Terahertz Science and Technology*, vol. PP, no. 99, pp. 1–3, 2018.
 - [17] J. L. Cano, A. Tribak, R. Hoyland, A. Mediavilla, and E. Artal, “Full band waveguide turnstile junction orthomode transducer with phase matched outputs,” *International Journal of RF and Microwave Computer-Aided Engineering*, vol. 20, no. 3, pp. 333–341, 2010.
 - [18] J. Campion, U. Shah, and J. Oberhammer, “Elliptical alignment holes enabling accurate direct assembly of micro-chips to standard waveguide flanges at sub-THz frequencies,” in *2017 IEEE MTT-S International Microwave Symposium (IMS)*, pp. 1262–1265, June 2017.
 - [19] B. Beurle, U. Shah, and J. Oberhammer, “Micromachined waveguides with integrated silicon absorbers and attenuators at 220–325 GHz,” in *Microwave Symposium (IMS), 2018 IEEE MTT-S International*, pp. 1–4, IEEE, 2018.
 - [20] D. Henke and S. Claude, “Minimizing RF performance spikes in a cryogenic orthomode transducer (OMT),” *IEEE Transactions on Microwave Theory and Techniques*, vol. 62, pp. 840–850, April 2014.